This is a preprint, the final version is subject to change, of the American Mineralogist (MSA)
Cite as Authors (Year) Title. American Mineralogist, in press.
DOI: https://doi.org/10.2138/am-2019-6921

Revision 2

Re-configuration and interaction of hydrogen sites in olivine at high temperature and high pressure

Yan Yang[1,*], Wendi Liu[1], Zeming Qi[2], ZhongPing Wang[3], Joseph R. Smyth[4], and Qunke Xia[1]

[1]Institute of Geology and Geophysics, School of Earth Sciences, Zhejiang University, Hangzhou 310027, China
[2]National Synchrotron Radiation Laboratory, University of Science and Technology of China, Hefei, Anhui 230026, China
[3]Department of Physics, University of Science and Technology of China, Hefei, Anhui 230026, China
[4]Department of Geological Sciences, University of Colorado, Boulder, Colorado 80309, U.S.A.

Corresponding author*
Institute of Geology and Geophysics
School of Earth Sciences
Zhejiang University
Hangzhou 310027, China
Email: yanyang2005@zju.edu.cn

ABSTRACT

Fingerprinting hydrogen storage sites in olivine at high temperature and high pressure is fundamental to understand water distribution and its impact on the upper mantle. We carried out *in situ* high temperature and high pressure IR spectroscopic investigations on hydrogen storage sites in the natural olivine and synthetic Fe-free forsterite. Based on *in situ* observations of hydrogen in both the natural olivine and synthetic Fe-free forsterite at high temperatures and pressures, we find that hydrogen does not transfer between storage sites with increasing temperature, but displays disordering at temperatures over 600 °C. In contrast, pressure can induce re-configuration of hydrogen storage sites corresponding to the 3610 and 3579 cm^{-1} bands. Hydrogen storage sites also exhibit disordering at high pressure. In addition, the dehydrogenation experiments of the natural olivine indicate interacts of hydrogen storage sites. Protons released from titanium-clinohumite defects move to pure Si vacancies, and also to Mg vacancies coupling with trivalent cations. This study is the

first attempt to fingerprint hydrogen storage sites in olivine at high temperature and high pressure using *in situ* IR spectroscopy. The implications of the temperature/pressure-induced disordering and re-configuration of hydrogen storage sites are discussed. The disordering and re-configuration of hydrogen storage sites at high temperature and high pressure favor better understanding water effects on physical properties of olivine. The interactions of hydrogen storage sites during dehydrogenation warn that some hydrogen if observed in dehydrated mantle-derived samples may not be original, and also make hydrogen diffusivity complex.

Keywords: Hydrogen sites, olivine, high temperature, high pressure, *In situ* IR spectroscopy, water, upper mantle

INTRODUCTION

Water as hydrogen defects can be incorporated and strongly influence physical properties of olivine (Karato 1990; Yang et al. 2015; Faul et al. 2016; Chang et al. 2017), thereby responsible for physical/chemical processes in the deep Earth (Peslier et al. 2010; Demouchy and Bolfan-Casanova 2016). However, the importance of water effects on some physical properties is still controversial (Wang et al. 2006; Yoshino et al. 2006; Costa and Chakraborty 2008; Fei et al. 2013; Faul et al. 2016; Cline II et al. 2018). One of the important reasons may be the complex hydrogen storage sites in olivine. At least four incorporation mechanisms of hydrogen have been identified in olivine (e.g., Beran and Putnis 1983; Berry et al. 2005, 2007a, 2007b; Walker et al. 2007): hydrogen in pure Si vacancies, hydrogen in Mg vacancies, hydrogen associated with titanium-clinohumite or trivalent cations in tetrahedral or octahedral sites. Recently, hydrogen linked to boron and fluoride in synthetic Fe-free forsterite and natural olivine also has been reported (Ingrin et al. 2014; Crépisson et al. 2014). Hydrogen with different incorporation mechanisms is expected to have different properties, such as diffusivities (Padrón-Navarta et al. 2014), infrared absorption coefficients (Kovàcs et al. 2010) and solubility (Ingrin et al. 2013; Padrón-Navarta and Hermann 2017). Thus, the water effects obtained from experiments in a regime where one mechanism is dominant may not be directly

compared to those where hydrogen is incorporated by a different mechanism. Consequently, understanding hydrogen storage sites in olivine is fundamental to explore water distribution at depth and its impact on mantle dynamics.

A principal advantage of Fourier-transform infrared (FTIR) spectroscopy is that it can fingerprint hydrogen of different incorporation mechanisms. Depending on the crystallographic environment, O-H stretching bands in the infrared spectra will have different frequencies. For example, hydrogen with different incorporation mechanisms has distinct absorption bands in the IR spectra of olivine: the bands at 3630-3400 cm^{-1} are assigned to hydrogen substituting for Si vacancies (e.g., Lemaire et al. 2004; Walker et al. 2007; Kovàcs et al. 2010; Umemoto et al. 2011); the bands at 3300-3100 cm^{-1} are assigned to hydrogen substituting for Mg vacancies (Berry et al. 2005; Lemaire et al. 2004; Walker et al. 2007); the two prominent bands at 3572 and 3525 cm^{-1} are assigned to hydrogen related to titanium-clinohumite defects (Berry et al. 2005, 2007a; Walker et al. 2007); the bands at 3400-3300 cm^{-1} are assigned to hydrogen coupled with trivalent cations substituting for Mg vacancies (Berry et al. 2007b). This current knowledge about hydrogen storage sites is mainly obtained from the IR spectra of olivine at ambient conditions. Since hydrogen is highly mobile, the migration of hydrogen between lattice sites at high temperature and high pressure may not be quenchable (Karato 2006). Therefore, there arises a question: whether the hydrogen storage sites in olivine obtained from IR spectra at ambient conditions are the same as those at the temperature and pressure conditions of the upper mantle? To answer this question and fingerprint hydrogen storage sites in olivine at high temperature and high pressure, *in situ* IR spectroscopic studies at high temperature and high pressure are indispensable.

To date, only one paper has reported the *in situ* IR spectra of hydrogen in olivine at high temperatures to 1100 °C (Yang and Keppler 2011). They suggested that hydrogen corresponding to the 3612 cm^{-1} band was not stable at high temperature based on its disappearance during heating. However, this explanation was challenged by the theoretical calculations on Fe-free forsterite (Balan et al. 2017; Qin et al. 2018),

who argued that a change in the defect geometry with temperature might explain the change of the 3612 cm^{-1} band without requiring proton migration. The samples used in Yang and Keppler (2011) were synthetic samples using natural olivine, while the calculations of Balan et al. (2017) and Qin et al. (2018) focused on hydrogen in Fe-free forsterite. In addition, except for one report of Raman spectra of hydrogen in Fe-free forsterite at high pressure (Hushur et al. 2009), no paper has reported *in situ* IR spectra of hydrogen in olivine at high pressures. To obtain more meaningful information of hydrogen storage sites in olivine at the temperature and pressure conditions of the upper mantle, in this study, we carry out *in situ* high temperature and high pressure IR spectroscopic experiments on natural olivine and synthetic Fe-free forsterite.

MATERIALS AND METHODS

Sample description

The natural olivine crystals are from peridotite xenocryst of the Udachnaya kimberlite pipe. The Fe-free forsterite (Fo_{100}) crystals (SZ0410B) were synthesized at Bayerisches Geoinstitut by Smyth et al. (2006). The synthesis was carried out in double-capsule experiments in the 5000 ton multi-anvil press at 12 GPa and 1400 °C. The chemical compositions of the natural olivine were determined using an EPMA 1600 (Shimadzu) electron microprobe at Zhejiang University (China). The analyses were performed with a 15 kV accelerating voltage, 10 nA beam current and a 5 μm beam diameter. Based on the multi-point measurements, the average compositions are as following: 41.6 wt. % SiO_2, 0.02 wt. % Al_2O_3, 0.04 wt. % CaO, 49.64 wt. % MgO, 0.06 wt. % MnO, 8.31 wt. % FeO, 0.05 wt. % Cr_2O_3, 0.35 wt. % NiO.

High temperature FTIR spectroscopy: *In situ* and quenched

Unpolarized and polarized FTIR spectra in the frequency range 4000-1000 cm^{-1} were collected using a Nicolet iS50 FTIR spectrometer coupled with a Continuμm microscope at Zhejiang University (China). A KBr beam-splitter and a liquid nitrogen-cooled MCT-A detector were used. A total of 128 scans were accumulated

for each spectrum at a 4 cm^{-1} resolution. The squared aperture size was set between 20×20 and 50×50 μm according to the sample size. Spectra were collected on the same selected area (core of the crystal) for each sample and background was collected at every temperature.

The natural olivine grain with 213 μm thickness and the synthetic Fe-free forsterite grain with 50 μm thickness were used for the *in situ* high temperature measurements. The natural olivine grain was from the polished peridotite section with random orientation. Both the natural olivine grain and the synthetic Fe-free forsterite grain are un-orientated. The sample was placed on a sapphire plate in an Instec HS1300 heating stage with CaF_2 windows. The heating stage was equipped with a resistance heater and an S-type thermocouple. The sample was heated in N_2 to avoid oxidation. The temperature was increased from 20 to 1000 °C using a rate of 15 ˚C/min. The sample temperature was determined with an uncertainty of less than 1 °C. For every temperature step, except otherwise indicated, the dwell time was 5 minutes.

To compare hydrogen preservation of different storage sites in natural olivine, dehydrogenation experiments were carried out on the natural olivine. Two grains with a thickness of 213 μm were annealed in the heating stage at a desired temperature of 800 and 1000 ˚C for different duration, respectively. To avoid oxidation by air, the heating stage was purged with N_2 flux of high purity during the annealing. Then IR measurements were carried out on the samples after quenching to room temperature. Spectra were collected on the same selected area for each sample.

In situ high pressure FTIR spectroscopy

The synchrotron infrared spectra from 4000-1000 cm^{-1} were collected at the Infrared spectroscopy and microscopic imaging beamline (BL01B) at the National Synchrotron Radiation Laboratory (University of Science and Technology of China), using a Bruker VERTEX 70V spectrometer coupled with a Bruker Hyperion 3000 microscope. A KBr beam-splitter and a liquid-nitrogen cooled MCT-A detector were applied. The aperture size was set to 30×30 μm. A total of 128 scans were

accumulated for each spectrum at a resolution of 4 cm^{-1}.

Hydrostatic high-pressure conditions were generated in a symmetric piston-cylinder-type diamond-anvil cell (DAC) with diamonds of 300 μm culet size. Prior to sample loading, a piece of stainless steel foil was pre-indented in the cell down to a thickness of ~20 μm. A 100 μm diameter hole was then drilled into the gasket. A thin sample section with 30 μm thickness was loaded into the sample chamber between two diamond anvils together with ruby for pressure calibration. The sample chamber was then filled with KBr as pressure medium. In the experiments, pressure variations within the samples were monitored with multiple ruby clips near the sample. At the peak pressures on compression, these variations did not exceed 10% of the total pressure.

Data analyses

To analyze site-specific temperature dependence of each OH band in the samples, the spectra were deconvoluted into Gaussian components using the Peakfit program (ver. 4.12, Systat Software Inc.). Width, amplitude and frequency of every single band were adjustable to obtain the best peak fitting. This method was also applied in previous studies (e.g., Zhang et al. 2007; Yang and Keppler 2011; Yang et al. 2015, 2019). The representative deconvolutions of the spectra are presented in the supplementary materials. Positions of the OH bands at elevated temperature and pressure are listed in Table 1. To obtain the site-specific diffusivities, areas of the OH bands after annealing for different duration are listed in Table 2. Based on dimensions of the samples, the site-specific hydrogen diffusivities were obtained using the one-dimensional model of diffusion from Ingrin et al. (1995). The ratio of the final to initial peak area was used to calculate the ratio of the final to initial concentration as a function of annealing duration.

RESULTS

IR spectra at ambient conditions

Polarized infrared spectra of the natural olivine and synthetic Fe-free forsterite collected at ambient conditions are illustrated in Figure 1. The spectra show the typical OH-related absorption bands. For the natural olivine, there are six OH bands at 3599, 3572, 3562, 3542, 3524 and 3482 cm^{-1}, with 3572 and 3524 cm^{-1} bands having a pleochroism different to the 3599, 3562, 3542 and 3484 cm^{-1} bands. For the synthetic Fe-free forsterite, there are five OH bands at 3610, 3579, 3566, 3552 and 3477 cm^{-1}, with 3566 and 3552 cm^{-1} bands having a pleochroism different to the 3610, 3579, and 3477 cm^{-1} bands. According to previous experimental studies, the OH bands at wavenumbers > 3400 cm^{-1} can be assigned to hydrogen in Si vacancies (Lemaire et al. 2004; Walker et al. 2007; Kovàcs et al. 2010). It should be noted that the two intense bands at 3572 and 3524 cm^{-1} in the natural olivine are typical of the mantle olivine (Berry et al. 2005). They are assigned to hydrogen related to titanium-clinohumite defects, which involves the formation of Si vacancies containing two hydrogen protons charge balanced by a Ti^{4+} cation occupying an adjacent octahedral site (Fig. 1c) (Berry et al. 2007a; Walker et al. 2007). The current theoretical studies on Fe-free forsterite further assigned the bands at wavenumbers > 3400 cm^{-1} to hydrogen in pure Si vacancies with different configurations (Umemoto et al. 2011; Xue et al. 2017; Qin et al. 2018). For example, the 3610, 3579, 3566, 3552 cm^{-1} bands are related to hydrogen with configuration 1, and the 3447 cm^{-1} band is related to hydrogen with configuration 4 (Fig. 1 in Umemoto et al. 2011). Since hydrogen occupies Si vacancies in both cases for pure Si vacancies and titanium-clinohumite defects, we use "titanium-clinohumite defect" indicating $MTiH_2O_4$ and "pure Si vacancies" indicates $M_2H_4O_4$ in this paper.

In situ high temperature IR spectra

Figure 2 shows evolutions of OH bands in the natural olivine at elevated temperatures up to 1000 °C. With increasing temperature, the OH bands broaden and shift. It can be clearly observed that the 3599 and 3572 cm^{-1} band progressively shift to lower frequencies while the 3524 cm^{-1} band does not shift with increasing temperature. At temperatures above 600 °C, the six OH bands completely overlap to

one broad band. This broad band does not shift any more, but drastically weakens with increasing temperature to 1000 °C. The six OH bands appear again in the spectrum of the sample quenched from 1000 °C, but with total absorbance decreasing. Moreover, different bands have distinct changes in their absorbances when comparing the spectrum before heating and after quenching. For example, the absorbances of the 3572 and 3524 cm^{-1} bands obviously reduce, while the absorbances of the 3599 and the 3542 cm^{-1} bands slightly increase.

Evolutions of OH bands in the synthetic Fe-free forsterite at elevated temperatures up to 1000 °C are illustrated in Figure 3. Similar to OH bands in the natural olivine, the five OH bands broaden with increasing temperature. But they exhibit more complex frequency shifts. With increasing temperature, the 3579 and 3552 cm^{-1} bands shift to lower frequencies, while the 3610 cm^{-1} band does not shift, and the 3477 cm^{-1} band shifts to higher frequencies. At temperatures above 600 °C, the OH bands completely overlap except the 3610 cm^{-1} band. These OH bands can be resolved again in the spectrum of the quenched sample from 1000 °C. In contrast to the natural olivine, no difference in OH absorbance has been found between the spectra of the Fe-free forsterite at 20 °C before and after quenching, indicating no dehydrogenation occurring during the heating process.

In situ high pressure IR spectra

Due to the low hydrogen content, IR spectra of the natural olivine in the DAC have a very poor ratio of signal to noise (see Fig. S1 in the supplementary materials). Therefore, the *in situ* high pressure IR spectra of OH in the natural olivine can not be measured in this study. Figure 4 displays the IR spectra of OH in the synthetic Fe-free forsterite at elevated pressures up to 10.96 GPa. Although there are interference fringes caused by multiple reflections between a sample and diamond surfaces in the spectra, the general evolutions can be clearly observed. Under compression, all the OH bands broaden. The 3610 and 3552 cm^{-1} bands shift to higher frequencies, while the 3579 and 3566 cm^{-1} bands shift to lower frequencies with increasing pressure. Except the 3610 cm^{-1} band, the other bands at 3579, 3566, 3552 and 3477 cm^{-1}

completely overlap at the pressures higher than 2.76 GPa. Furthermore, the absorbance of the 3610 cm^{-1} band increases while decreases for the 3579 cm^{-1} band with increasing pressure. All the changes are reversible when comparing the spectrum before and after compression.

IR spectra of the natural olivine after annealing

Evolutions of the polarized IR (E//a) spectra of the natural olivine after being quenched from 800 °C with annealing duration are shown in Figure 5. The intensities of the 3572 and 3524 cm^{-1} OH bands significantly reduce with annealing duration, while slightly increases for the 3599 and 3542 cm^{-1} OH bands. Interestingly, the new bands at 3356 and 3327 cm^{-1} appear with increasing duration. To explore the origin of these new bands, we compare the IR spectra of the natural olivine after annealing for 15 minutes at different temperatures (Fig. 5). The spectrum of the sample after annealing at 500 °C is the same as before annealing, indicating that dehydrogenation did not occur at this temperature range. After annealing at 800 and 1000 °C, the intensities of the 3572 and 3524 cm^{-1} OH bands decrease, the intensities of the 3599 and 3542 cm^{-1} band increase, and the new bands at 3356 and 3327 cm^{-1} appear in the spectra. Thus, the occurrence of the new OH bands may be new hydrogen defects related to dehydrogenation of hydrogen corresponding to titanium-clinohumite defects (3572 and 3524 cm^{-1} OH bands).

DISCUSSION

Disordering of hydrogen sites at high temperature

To quantitatively address hydrogen storage sites at high temperature, we plot frequencies of OH bands in the natural olivine and synthetic Fe-free forsterite as a function of temperature in Figure 6. The data of the synthetic olivine from Yang and Keppler (2011) were included for comparison.

For the natural olivine, the 3599 cm^{-1} band which is assigned to hydrogen in pure Si vacancies ($M_2H_4O_4$) shifts to lower frequencies with increasing temperature. The

3572 and 3524 cm^{-1} bands which correspond to hydrogen related to titanium-clinohumite defects ($MTiH_2O_4$) exhibit different frequency shifts. The 3572 cm^{-1} band progressively shifts to lower frequencies with increasing temperature to 800 °C, while the 3524 cm^{-1} band frequency seems insensitive to temperature at least up to 600 °C. The negative frequency shifts (shift to lower frequency with increasing temperature) of the 3599 and 3572 cm^{-1} OH bands indicate temperature-induced lengthening and weakening of O-H bonds. The little shift of the 3524 cm^{-1} band suggests that the corresponding O-H bond cannot be easily influenced by temperature. Therefore, although both the 3572 and 3524 cm^{-1} bands are assigned to hydrogen related to titanium-clinohumite defects, their O-H bonds have different local environments. By extrapolation from the evolutions, it can be expected that hydrogen of titanium-clinohumite defects should have O-H bonds with similar strength at temperatures of the upper mantle. Figure 6 suggests that the tendencies of the 3599 and 3572 cm^{-1} band shifts with increasing temperature are similar between the natural olivine of this study and the synthetic olivine in Yang and Keppler (2011). Thus, the "M" type of experiment introducing H into pre-existing crystals (metastable equilibrium, Tollan et al. 2018) of the synthesis of olivine used in Yang and Keppler (2011) at least preserves the information of hydrogen storage sites related to pure Si vacancies and titanium-clinohumite defects of the natural sample. In addition, the synthetic olivine in Yang and Keppler (2011) contains other hydrogen storage sites, which are not observed in the natural olivine in this study.

The OH bands related to pure Si vacancies of the synthetic Fe-free forsterite are different to the natural olivine, probably corresponding to different configurations of hydrogen (Umemoto et al. 2011; Blanchard et al. 2017). Hydrogen in Si vacancies with different configurations has different temperature dependences. Similar to the 3612 cm^{-1} band of the synthetic olivine in Yang and Keppler (2011), the 3610 cm^{-1} band does not shift with increasing temperature. However, the 3579 and 3552 cm^{-1} shift to lower frequencies, and the 3477 cm^{-1} band shift to higher frequencies. According to previous studies (Umemoto et al. 2011; Xue et al. 2017; Qin et al. 2018),

the 3610, 3579 and 3552 cm^{-1} bands are related to hydrogen in Si vacancies with configuration 1, and the 3477 cm^{-1} band is related to hydrogen in Si vacancies with configuration 4. In the configuration 1, one proton (O2-H) is different from the other three protons, pointing away from the $(4H)_{Si}O_4$ tetrahedron. The different temperature dependences between the 3612 cm^{-1} band and the other two bands at 3579 and 3552 cm^{-1} can thus be explained by their different pointing directions. The thermal expansion of tetrahedron may have little impact on the O2-H which points away from the tetrahedron, thereby the O-H bond is not sensitive to temperature. In contrast, the other O-H bonds in the configuration 1 lengthen with temperature-induced expansion of the tetrahedron, and the corresponding OH bands exhibit negative frequency shifts. In configuration 4, four protons locate close to the surface of the $(4H)_{Si}O_4$ tetrahedron, with O1-O2 forming the relatively stronger hydrogen bonding (O-H…O, an attractive interaction between a hydrogen atom from a hydroxyl (O-H) group and a near neighbor oxygen atom). Previous work suggested that weakening of hydrogen bonds (O-H…O) will induce a relative strengthening of the primary O-H bonds (Nakamoto et al. 1955; Xu et al. 2013). Thus, the positive frequency shift (shift to higher frequencies with increasing temperature) of the 3477 cm^{-1} band can be explained by the lengthening and weakening of hydrogen bonds (O1-O2).

It has been reported that a negative relation exists between the temperature dependence of OH frequencies and their initial frequencies for pyroxene and garnet (Lu and Keppler 1997; Yang et al. 2010, 2012, 2015, 2019). However, we do not find any relationship between the temperature-induced frequency shifts of OH bands and their initial frequencies based on our data in Figure 6. It should be noted that most OH bands correspond to hydrogen related to pure Si vacancies in this study. The multiple configurations of hydrogen in pure Si vacancies may disturb that relationship. Excluding the hydrogen in pure Si vacancies, the negative relationship still exists for hydrogen related to titanium-clinohumite defects and Mg vacancies. For example, the 3572 cm^{-1} band has a negative frequency shift and the 3524 cm^{-1} band has zero frequency shift for the natural olivine in this study, while the 3178 and 3151 cm^{-1}

318 bands corresponding to Mg vacancies have positive frequency shifts for the synthetic
319 Fe-free forsterite (Ingrin et al. 2013).

320 For the natural olivine, the six OH bands corresponding to hydrogen related to
321 pure Si vacancies and titanium-clinohumite defects are resolved at ambient
322 temperature. With increasing temperatures over 600 °C, one broad band exists. The
323 one broad band at high temperature can arise from a statistical distribution of
324 hydrogen across multiple environments or hydrogen disordering in the olivine
325 structure. By extrapolating to a temperature of 1000 °C from the linear relationship in
326 Figure 6, the 3599 cm^{-1} band will shift to 3572 cm^{-1}, the 3572 cm^{-1} band will shift to
327 3537 cm^{-1}, and the 3524 cm^{-1} band will remain at this frequency. Some constraints on
328 the hydrogen bonding (O-H…O) environments at room temperature and at 1000 °C
329 can be provided, according to the relationship between OH frequency and O-O
330 distance (Libowitzky 1999). The predicted O-O distances at 1000 °C for the three OH
331 bands are similar, about 3.1 Å, 3.0 Å and 2.9 Å, respectively. Thus, the single broad
332 band observed at high temperature (1000 °C) is interpreted here as
333 temperature-induced hydrogen disordering across multiple bonding sites with similar
334 O-O distances. For the synthetic Fe-free forsterite, the five OH bands corresponding
335 to hydrogen in pure Si vacancies with different configurations are also resolved at
336 ambient temperature. With increasing temperature up to 1000 °C, the 3610 cm^{-1} band
337 is still distinguishable, which is in contrast to the conclusion by Yang and Keppler
338 (2011) that this band is not stable at high temperature. Similar to the OH bands in the
339 natural olivine, the other OH bands overlap at high temperatures, indicating hydrogen
340 disordering between different configurations. Temperature or pressure-induced
341 hydrogen disordering was also expected in the structures of wadsleyite and
342 ringwoodite (Kohn et al. 2002; Panero et al. 2013).

343 **Disordering and re-configuration of hydrogen sites at high pressure**

344 Due to the low hydrogen concentration in the natural olivine and the poor signal
345 to noise ratio of the spectra in DAC, we can not explore hydrogen storage sites in it at
346 high pressure. Nevertheless, variations of hydrogen storage sites in pure Si vacancies

of the synthetic Fe-free forsterite at high pressure can be deciphered from the IR spectra. Figure 7 shows the frequency shifts of some prominent OH bands with increasing pressure. The 3610 cm^{-1} band shifts to higher frequencies. However, Hushur et al. (2009) reported that the 3610 cm^{-1} band shifted to lower frequencies at pressures below 10 GPa and then to higher frequencies at pressures higher than 10 GPa. From the Raman spectra in Hushur et al. (2009), we noticed that the intensity signals of this band are very weak, and only three data points are presented for OH frequency as a function of pressure below10 GPa, probably hindering the extrapolation of frequency shift with pressure. The positive frequency shift of the 3610 cm^{-1} band is in agreement with compression of the corresponding O-H bonds. In contrast, this O-H bond is not sensitive to temperature as stated before. In agreement with Hushur et al. (2009), the 3579 and 3566 cm^{-1} bands shift to lower frequencies with increasing pressure. The 3552 cm^{-1} band shifts to higher frequencies under compression, which is contrary to the temperature effect. Thus, this band shift may be caused by the compression of the O-H bonds. It is generally expected that pressure and temperature should have antagonistic effects. However, it is not the case for the 3579 cm^{-1} band in this study. Pressure and temperature have similar effects on the 3579 cm^{-1} band, with negative frequency shift. Therefore, the frequency shift of the 3579 cm^{-1} band with pressure may not be simply interpreted from the variations of O-H bonding length. It also depends on bond angle (Hofmeister et al. 1999).

In addition to frequency shifts, intensities of the observed OH modes also change under compression. With increasing pressure, the intensity of the 3610 cm^{-1} band increases, while the 3579 cm^{-1} band weakens. The intensity ratio of the two bands increases with increasing pressure (Fig. 7). Hushur et al. (2009) also observed this feature from the Raman spectra of Fe-free forsterite at elevated pressures. They suggested that exchange of hydrogen likely occurred between the octahedral and tetrahedral sites. As mentioned above, the 3610 and 3579 cm^{-1} bands are assigned to hydrogen in pure Si vacancies of configuration 1, with different O-H pointing directions. Thus, these results may indicate that pressure can induce exchange of

hydrogen in the pure Si vacancies of configuration 1. This hydrogen exchange is not observed from the IR spectra at elevated temperatures. Moreover, as in the case of the OH bands at high temperatures, the bands lower than 3600 cm^{-1} also overlap at high pressures, indicating hydrogen disordering in the pure Si vacancies. As a result, it can be inferred that at the temperature and pressure of the upper mantle, hydrogen related to the 3610 cm^{-1} band should be predominant, with disordering of hydrogen corresponding to the other OH bands. Of course, this is just the case for the disordering and re-configuration of hydrogen in the pure Si vacancies of the synthetic Fe-free forsterite with increasing pressure. It is a pity that we do not observe behavior of other hydrogen storage sites during compression because of the limited samples in this study. In view of the distinct hydrogen storage sites between olivine and its high-pressure polymorph wadsleyite, it may be expected that pressure will induce re-distribution of hydrogen storage sites in olivine, especially during transition to the high-pressure polymorph. To test this conjecture, it should consider how the content varies between different hydrogen defects (e.g., pure Si vacancies, titanium-clinohumite defects and Mg vacancies) as a function of pressure in future.

Interaction of hydrogen sites during dehydrogenation

Based on the dehydrogenation experiments on Ti-doped, Fe-free forsterite, Padrón-Navarta et al. (2014) have reported that the mobility of hydrogen through the proton-vacancy mechanism depends on the type of substitution mechanism, with hydrogen diffusing through the tetrahedral sites significantly slower than through octahedral sites. The recent study on naturally hydrated olivine argued that the OH bands at 3650-3500 cm^{-1} yield similar hydrogen diffusivities, except for one band at 3598 cm^{-1}, which yields slower hydrogen diffusivity than the others (Thoraval et al. 2018). The dehydrogenation experiments on the natural olivine from the upper mantle in this study also reveal different dehydrogenation rates for different incorporation mechanisms (Fig. 5). We plotted absorbances of the deconvoluted bands with annealing duration at 800 °C in Figure 8. With annealing duration, the integral absorbance of the 3599 and 3542 cm^{-1} bands abnormally increase, and the integral

absorbances of the 3572 and 3524 cm^{-1} bands decrease. We exclude possible changes induced by distinctive absorption along different O-H directions based on the following reasons: First, in this study, the sample was annealed in the heating stage and was not rotated; Second, the polarized IR spectra were collected on the same selected point after quenching the sample to room temperature, with rotating the polarizer to the same angle. Thus, the variations of the integral absorbance shown by Figure 8 reflect dehydrogenation and hydration of the hydrogen storage sites. As stated before, the 3599 and the 3542 cm^{-1} bands are assigned to hydrogen in pure Si vacancies, while the 3572 and 3524 cm^{-1} bands correspond to hydrogen related to titanium-clinohumite defects. Therefore, the increase of the integral absorbances of the 3599 and 3542 cm^{-1} band indicates hydration of the pure Si vacancies. In contrast, the decrease of the integral absorbances of the 3572 and 3524 cm^{-1} band suggests dehydrogenation of the titanium-clinohumite defects. To have an approximated idea about the site-specific hydrogen diffusivity, dehydrogenation rates of the titanium-clinohumite defects were fitted to be on the order of 10^{-13} m^2 s^{-1} (Fig. 8).

It has been shown that, hydrogen mobility is governed by two mechanisms at moderate pressure (< 1 GPa) (e.g., Mackwell and Kohlstedt 1990; Demouchy and Mackwell 2006). One is proton-polaron mechanism, which is fast and involves redox reaction (Fe^{2+}-Fe^{3+}). The other is proton-vacancy mechanism, which is slower than the first and involves cationic vacancies. At low temperature (< 1000 °C) or short time, proton-polaron mechanism is the first mechanism to lead H incorporation, while proton-vacancy mechanism is dominant at higher temperature (> 1000 °C) or longer time. In this study, the dehydrogenation experiments were processed at 800 °C for short time of 270 min. The hydrogen diffusivity (10^{-13}) of the titanium-clinohumite defects at 800 °C is in accordance with the hydrogen diffusivity with proton-polaron mechanism. Furthermore, the color of the sample was changed from green to brown with dehydrating. Thus, the mechanism most likely happening in the dehydrogenation experiments of this study is proton-polaron mechanism. Our study shows that there exist interactions between different hydrogen defects. The hydrogen related to

titanium-clinohumite defects moves to the pure Si vacancies (from $MTiH_2O_4$ to $M_2H_4O_4$), giving rise to the increase and decrease of hydrogen in pure Si vacancies and hydrogen related to titanium-clinohumite defects, respectively. These processes propose an interpretation at atomic level to the slowest diffusivity of the 3598 cm^{-1} band observed by previous study (Thoraval et al. 2018). Hydrogen redistributes not only between pure Si vacancies and titanium-clinohumite defects, but also from titanium-clinohumite defects to newly created hydrogen storage sites. For example, the new bands at 3356 and 3327 cm^{-1} occur, co-existing with dehydrogenation of the titanium-clinohumite defects (Fig. 5). The bands at 3356 and 3327 cm^{-1} are typical of hydrogen coupled with trivalent cations in Mg vacancies. Nevertheless, coupling with which trivalent cation is still in debate. For example, Berry et al. (2005) suggested that these bands are associated with Fe^{3+} in mantle-derived olivine. Al was also proposed as one of the trivalent cations contributing to this hydrogen storage sites by Berry et al. (2007b). Tollan et al. (2015) demonstrated that a combination of Cr and Fe are most likely responsible for this hydrogen site in upper mantle olivine. The very recent work by Tollan et al. (2018) reported a previously unrecognized role for Na in incorporation of this hydrogen site in natural olivine. Our study found that the occurrence of this hydrogen defect is related to the dehydrogenation of the titanium-clinohumite defects. Since dehydrogenation of the Fe-bearing natural olivine usually involves oxidation of Fe^{2+} to Fe^{3+}. The dehydrogenation mechanism of this study also supports the oxidation of Fe^{2+} to Fe^{3+}. Thus, the new bands at 3356 and 3327 cm^{-1} in this study should be diffusion of hydrogen to M site charge-balanced by ferric iron formed during dehydrogenation, in agreement with Berry et al. (2005).

Interestingly, the very recent study also reported redistribution between hydrogen storage sites in the olivine from Kilauea Iki (Ferriss et al. 2018). They found that the [Fe3+-H] peak intensity clearly decreased, while the pure Si vacancies peak intensity increased after 8 hour at 800 °C. Although the reactions between sites reported in Ferriss et al. (2018) are different from our study, both studies revealed the interactions of hydrogen storage sites. Conclusively, the interaction of the hydrogen storage sites

in olivine makes the path of a proton released from the crystal complex, results in non-inherent hydrogen diffusivity changing with progressive dehydrogenation, and makes the judgment of the original hydrogen storage sites in olivine at the upper mantle conditions difficult.

IMPLICATIONS

Although knowledge about water distributions and its cycle in the deep Earth has achieved great progress (e.g., Peslier 2010; Demouchy and Bolfan-Casanova 2016; Peslier et al. 2017; Xia et al. 2018), the importance of water effects on physical properties in the deep Earth is still controversial. Different hydrogen storage sites have distinct impacts on the host minerals. However, most studies merely determine a total water content and do not distinguish different hydrogen storage sites in their samples. Obviously, this does not benefit the understanding of the effects of water in the deep Earth. For olivine, the most important upper mantle mineral, hydrogen storage sites have been extensively studied (e.g., Berry et al. 2005, 2007a, 2007b; Walker et al. 2007; Umemoto et al. 2011; Xue et al. 2017; Qin et al. 2018). Since the conditions of the upper mantle are not the same as ambient conditions, and most experiments of water effects on mineral properties are carried out at high temperature and high pressure, it is indispensable to know hydrogen storage sites in olivine at high temperature and high pressure. Although assignments of some OH bands to Si vacancies or Mg vacancies in olivine are still controversial (e.g., Smyth et al. 2006; Walker et al. 2007), our study focuses on variations of the OH bands with temperature and pressure. We report disordering and re-configuration of hydrogen storage sites at high temperature and high pressure, and also interactions of hydrogen storage sites during dehydrogenation. These are vital for understanding water impacts on the deep Earth.

Implications of disordering and re-configuration of hydrogen sites at high temperature and pressure

Dai and Karato (2014) showed by experiment that the mechanism of electrical

conductivity of olivine changed with temperature. Based on the model of Karato (2013), they proposed that diffusion of hydrogen in Mg site is the dominant contribution to electrical conductivity at high temperatures (> 900 K), while free protons will dominant at low temperatures. IR spectra are efficient tracers for local environments of hydrogen defects. If free protons at low temperatures transfer to hydrogen in Mg sites at high temperatures, it is expected to be observed from the *in situ* IR spectra at elevated temperatures. In the IR spectra of both natural olivine and synthetic Fe-free forsterite from 20 to 1000 °C, we do not find the growth of OH bands corresponding to hydrogen in Mg sites with increasing temperature. This suggests that free protons do not transfer easily to bond to oxygen in Mg sites in olivine for the temperature range in this study. However, the local environments of hydrogen storage sites indeed change with increasing temperature. At temperatures over 600 °C, hydrogen storage sites of pure Si vacancies and titanium-clinohumite defects in the natural olivine have similar O-O distances and display disordering in the structure. Moreover, except the hydrogen site in pure Si vacancies with O-H pointing away from the Si tetrahedron, hydrogen storage sites in pure Si vacancies with distinct configurations in the synthetic Fe-free forsterite also exhibit disordering at temperatures above 600 °C. At high temperature, the strength of bonding between protons and the surrounding atoms are similar among different hydrogen storage sites. The protons belonging to different sites should thereby have similar mobility at high temperature (e.g., > 600°C), but this is likely not the case at low temperature. Thus, it is unlikely that the degree of hydrogen disorder in samples quenched to room temperature is the same as that at high temperature. Just as stated in Kohn et al. (2002), although it is now difficult to predict the effect of different degrees of hydrogen ordering on physical properties, it should be taken into account when predicting and extrapolating data on physical properties from room temperature measurements. Therefore, the different local environments of hydrogen defects between high temperature and low temperature may be responsible for the different activation enthalpy of electrical conductivity between high and low temperature experiments observed by Dai and Karato (2014).

Pressure and temperature will control hydrogen storage sites in the deep Earth. Nevertheless, it is generally accepted that temperature and pressure have competing effects on O-H bonds. However, this study observed that O-H bond of the 3579 cm^{-1} band displays the same response to temperature and pressure. Additionally, the O-H bond of the 3610 cm^{-1} band seems insensitive to temperature but quite sensitive to pressure. At the temperature and pressure conditions of the upper mantle, except the 3610 cm^{-1} band, hydrogen storage sites of the other OH bands display disordering. Most importantly, pressure can induce exchange of hydrogen in the Si vacancies of configuration 1 with different pointing directions. At pressures higher than 2.76 GPa, hydrogen site corresponding to the 3610 cm^{-1} is predominant. The disorder and re-configuration of hydrogen storage sites may impact elastic properties of olivine, which deserve further investigation. In light of the results of this study, it will be important to account for these changes at high temperature and pressure when understanding the difference between elastic properties measured at ambient and upper mantle conditions. Indeed, Mao et al. (2010) observed that the elastic wave velocity of hydrogen-bearing Fe-free forsterite is slightly lower than that of the anhydrous forsterite at 1-bar pressure, while a sound velocity crossover occurs around 3-4 GPa. The pressure range of the crossover occurring is consistent with the pressure at which disordering and re-configuration between hydrogen storage sites happened in this study. Several seismic features interpreted as discontinuities have been reported in the upper mantle (e.g., Kawakatsu et al. 2009; Rychert and Shearer 2009; Tauzin et al. 2010; Beghein et al. 2014; Hopper and Fischer 2015; Wei and Shearer 2017). However, it is difficult to explain these discontinuities at low temperatures (<1000 °C) based on current models (Karato and Park 2019). Thus, to better constrain water effects on the elastic properties of olivine and further seismic discontinuities of the upper mantle, it is very important to perform simultaneously high P-T measurements, which is still very limited and challenging (see Mao et al. 2016 for a review).

Implications of interactions of hydrogen sites during dehydrogenation

The interactions of the hydrogen storage sites in olivine during dehydrogenation

make the understanding and estimation of the original hydrogen in olivine at the upper mantle conditions difficult. It has been suggested that titanium-clinohumite defect is the most important hydrogen storage site typical of natural olivine in the upper mantle (Berry et al. 2005). Furthermore, the hydrogen of titanium-clinohumite defect strongly enhances deformation in the dislocation and diffusion creep regime, thereby can play an important role for rheology of the upper mantle (Faul et al. 2016). Because of the relatively quick dehydrogenation rate of water corresponding to this defect, we usually observe low amounts of hydrogen in the natural mantle-derived samples, which may be tip of the iceberg of hydrogen of the titanium-clinohumite defects in olivine of the upper mantle. This study finds that the lost hydrogen of the titanium-clinohumite defects does not completely release out of the crystal. It can migrate to pure Si vacancies, and also can move to trivalent cation defects. Additionally, Ferriss et al. (2018) also revealed the interactions of hydrogen storage sites in the natural olivine: hydrogen in pure Si vacancies may be inherited from [Fe^{3+}-H] (trivalent cation defects). Therefore, dehydrogenation and interactions of hydrogen storage sites may be very complex. There may be other reactions among storage sites during dehydrogenation, depending on the chemical compositions, hydrogen storage sites and the annealing conditions.

The interactions of hydrogen storage sites should call our attention to further understanding of hydrogen in the mantle. For example, hydrogen of pure Si vacancies may be partly inherited from hydrogen of titanium-clinohumite defects suggested by this study, or trivalent cation defects suggested by Ferriss et al. (2018). Dehydrogenation of other sites can induce hydration of the pure Si vacancies, thus, supporting the dominant role of pure Si vacancies for hydrogen in olivines at high temperature and high pressure. Moreover, hydrogen of trivalent cation defects may not be original either. It is related to diffusion of hydrogen to M site charge-balanced by ferric iron formed during dehydrogenation. Indeed, Grant et al. (2007) reported the relationship between hydrogen associated with trivalent cation defects and oxygen fugacity. Therefore, the occurrence of this band if observed in some natural olivine

might be used as a marker of oxidizing conditions, and also a previous dehydrogenation of other hydrogen storage sites. Since OH bands of different hydrogen storage sites in olivine have different IR absorption coefficients (Kovàcs et al. 2010), the interactions of different hydrogen storage sites call into question whether the hydrogen contents and storage sites observed in mantle xenoliths brought up in alkali and kimberlitic magmas are truly intrinsic. Additionally, the interaction of the hydrogen storage sites in olivine makes the path of a proton released from the crystal complex and results in complex hydrogen diffusivities. One should therefore be cautious when modeling olivine water storage capacity or bulk mantle water content based only on samples containing these features.

ACKNOWLEDGEMENTS

This work is supported by the Strategic Priority Research Program (B) of Chinese Academy of Sciences (XDB18000000), the Zhejiang Province Natural Science Foundation of China (LY18D020001), and Infrared spectroscopy and microscopic imaging beamline (BL01B) of National Synchrotron Radiation Laboratory at the University of Science and Technology of China (2018-HLS-PT-001339, 2018-HLS-PT-001428). Joseph R. Smyth acknowledges support from US National Science Foundation (Grant No. EAR14-16979). We thank Sylvie Demouchy for handling the manuscript, and Peter Tollan and an anonymous reviewer for their comments.

References

Asimow, P.D., Stein, L.C., Mosenfelder, J.L., and Rossman, J.R. (2006) Quantitative polarized infrared analysis of trace OH in populations of randomly oriented mineral grains. American Mineralogist, 91, 278-284.

Balan, E., Blanchard, M., Lazzeri, M., and Ingrin, J. (2017) Theoretical Raman spectrum and anharmonicity of tetrahedral OH defects in hydrous forsterite.

606 European Journal of Mineralogy, 29, 201-212.

607 Beghein, C., Yuan, K., Schmerr, N., and Xing, Z. (2014) Changes in seismic
608 anisotropy shed light on the nature of the Gutenberg discontinuity. Science, 343,
609 1237-1240.

610 Beran, A., and Putnis, A. (1983) A model of the OH position in olivine, derived from
611 infrared spectroscopy investigations. Physics and Chemistry of Minerals, 9,
612 57-60.

613 Berry, A., Hermann, J., O'Neill, H.S.C., and Foran, G.J. (2005) Fringerprinting the
614 water site in mantle olivine. Geology, 33, 869-872.

615 Berry, A., Walker, A.M., Hermann, J., O'Neill, H.S.C., Foran, G.J., and Gale, J.
616 (2007a) Titanium substitution mechanisms in forsterite. Chemical Geology, 242,
617 176-186.

618 Berry, A., O'Neill, H.S.C., Hermann, J., and Scott, D.R. (2007b) The infrared
619 signature of water associated with trivalent cations in olivine. Earth and
620 Planetary Science Letters, 261(1-2), 134-142.

621 Blanchard, M., Ingrin, J., Balan, E., Kovàcs, I., and Withers, A.C. (2017) Effect of
622 iron and trivalent cations on OH defects in olivine. American Mineralogist, 102,
623 302-311.

624 Chang, Y.Y., Hsieh, W.P., Tan, E., and Chen, J.H. (2017) Hydration-reduced lattice
625 thermal conductivity of olivine in Earth's upper mantle. Proceedings of the
626 National Academy of Sciences of the United States of America, 114, 4078.

627 Cline, II., Faul, U.H., David, C.E., Berry, A.J., and Jackson, I (2018) Redox
628 influenced seismic properties of upper-mantle olivine. Nature, 555, 355-358.

629 Costa, F., and Chakraborty, S. (2008) The effect of water in Si and O diffusion rates in
630 olivine and implications for the transport properties and processes in the upper
631 mantle. Physics of the Earth and Planetary Interiors, 166, 11-29.

632 Crépisson, C., Blanchard, M., Bureau, H., Sanloup, C., Withers, A.C., Khodja, H.,

633 Surblé, H., Raepsaet, C., Béneut, K., Leroy, C., Giura, P., and Balan, E. (2014)
634 Clumped fluoride-hydroxyl defects in forsterite: Implications for the
635 upper-mantle. Earth and Planetary Science Letters, 390, 287-295.

636 Dai, L., and Karato, S. (2014) High and highly anisotropic electrical conductivity of
637 the asthenosphere due to hydrogen diffusion in olivine. Earth and Planetary
638 Science Letters, 408, 79-86.

639 Demouchy, S., and Mackwell, S. (2006) Mechanisms of hydrogen incorporation and
640 diffusion in iron-bearing olivine. Physics and Chemistry of Minerals, 33,
641 347-355.

642 Demouchy, S., and Bolfan-Casanova, N. (2016) Distribution and transport of
643 hydrogen in the lithospheric mantle: A review. Lithos, 240-243, 402-425.

644 Faul, U., Cline, C.J., David, E.C., Berry, A.J., and Jackson, I. (2016)
645 Titanium-hydroxyl defect-controlled rheology of the Earth's upper mantle. Earth
646 and Planetary Science Letters, 452, 227-237.

647 Fei, H., Wiedenbeck, M., Yamazaki, D., and Katsura, T. (2013) Small effect of water
648 on uppermantle rheology based on silicon self-diffusion coefficients. Nature,
649 213-215.

650 Ferriss, E., Plank, T., Newcombe, M., Walker, D., and Hauri, E. (2018) Rates of
651 dehydration of olivines from San Carlos and Kilauea Iki. Geochimica
652 Cosmochimica Acta, 242, 165-190.

653 Grant, K. J., Brooker, R. A., Kohn, S. C., and Wood, B. J. (2007). The effect of
654 oxygen fugacity on hydroxyl concentrations and speciation in olivine:
655 Implications for water solubility in the upper mantle. Earth and Planetary
656 Science Letters, 261(1-2), 217-229.

657 Hofmeister, A.M., Cynn, H., Burnley, P.C., and Meade, C. (1999) Vibrational spectra
658 of dense, hydrous magnesium silicates at high pressure: importance of the
659 hydrogen bond angle. American Mineralogist, 84, 454-464.

660 Hopper, E., and Fischer, K.M. (2015) The meaning of midlithospheric discontinuities:

A case study in the northern U.S. craton. Geochemistry Geophysics Geosystems, 16, 4057-4083.

Hushur, A., Manghnani, M.H., Smyth, J.R., Nestola, F., and Frost, D.J. (2009) Crystal chemistry of hydrous forsterite and its vibration properties up to 41 Gpa. American Mineralogist, 94, 751-760.

Ingrin, J., Hercule, S., and Charton, T. (1995) Diffusion of hydrogen in diopside: Results of dehydration experiments. Journal of Geophysical Research, 100, 15489-15499.

Ingrin, J., Liu, J., Depecker, C., Kohn, S.C., Balan, E., Grant, K.J. (2013) Low temperature evolution of OH bands in synthetic forsterite, implication for the nature of H defects at high pressure. Physics and Chemistry of Minerals, 40, 499-510.

Ingrin, J., Kovács, I., Deloule, E., Balan, E., Blanchard, M., Kohn, S.C., and Hermann, J. (2014) Identification of hydrogen defects linked to boron substitution in synthetic forsterite and natural olivine. American Mineralogist, 99, 2138-2141.

Karato, S. (1990) The role of hydrogen diffusivity in the electrical conductivity of the upper mantle. Nature, 347, 272-273.

Karato, S. (2006) Influence of hydrogen-related defects on the electrical conductivity and plastic deformation of mantle minerals: a critical review. In Earth's Deep Water Cycle vol. 168, American Geophysical Union, Washington D.C.

Karato, S. (2013) Theory of isotope diffusion in a material with multiple species and its implications for hydrogen-enhanced electrical conductivity in olivine. Physics of Earth Planetary Interiors, 219, 49-54.

Karato, S., and Park, J. (2019) On the Origin of the Upper Mantle Seismic Discontinuities. In Lithospheric Discontinuities, Geophysical Monograph vol. 239. American Geophysical Union. Published 2019 by John Wiley & Sons, Inc.

687 Kawakatsu, H., Kumar, P., Takei, Y., Shinohara, M., Kanazawa, T., Araki, E., and
688 Suyehiro, K. (2009) Seismic evidence for sharp lithosphere-asthenosphere
689 boundaries of oceanic plates, Science, 324, 499-502.

690 Kohn, S.C., Brooker, R.V., Frost, D.J., Slesinger, A.E., and Wood, B.G. (2002)
691 Ordering of hydroxyl defects in hydrous wadsleyite (β-Mg_2SiO_4). American
692 Mineralogist, 87, 293-301.

693 Kovàcs, I., O'Neill, H.S.C., Hermann, J., and Hauri, E.H. (2010) Site-specific infrared
694 O–H absorption coefficients for water substitution into olivine. American
695 Mineralogist, 95, 292-299.

696 Lemaire, C., Kohn, S.C., and Brooker, R.A. (2004) The effect of silica activity on the
697 incorporation mechanisms of water in synthetic forsterite: a polarised infrared
698 spectroscopic study. Contributions to Mineralogy and Petrology, 147, 48-57.

699 Libowitzky, E. (1999) Correlation of O-H stretching frequencies and O-H…O
700 hydrogen bond lengths in minerals. Monatshefte für Chemie, 130, 1047-1059.

701 Lu, R., and Keppler, H. (1997) Water solubility in pyrope in 100 kbar. Contributions
702 to Mineralogy and Petrology, 129, 35-42.

703 Mackwell, S.J., and Kohlstedt, D.L. (1990) Diffusion of hydrogen in olivine:
704 implications for water in the mantle. Journal of Geophysical Research, 95,
705 5079-5088.

706 Mao, Z., and Li, X.Y. (2016). Effect of hydration on the elasticity of mantle minerals
707 and its geophysical implications. Science China, 5, 873-888.

708 Mao, Z., Jacobsen, S.D., Jiang, F., Smyth, J.R., Holl, C.M., Frost, D.J., and Duffy, T.S.
709 (2010) Velocity crossover between hydrous and anhydrous forsterite at high
710 pressures. Earth and Planetary Science Letters, 293, 250-258.

711 Nakamoto, K., Margosches, M., and Rundle, R.E. (1955) Stretching frequencies as a
712 function of distances in hydrogen bonds. Journal of the American Chemical
713 Society, 77, 6480-6486.

714 Padrón-Navarta, J.A., Hermann, J., and O'Neill, H.S.C. (2014) Site-specific hydrogen
715 diffusion rates in forsterite. Earth and Planetary Science Letters, 392, 100-112.

716 Padrón-Navarta, J.A., and Hermann, J. (2017) A subsolidus olivine water solubility
717 equation for the Earth's upper mantle. Journal of Geophysical Research-Solid
718 Earth, 122, 9862-9880.

719 Panero, W.R., Smyth, J.R., Pigott, J.S., Liu, Z., and Frost, D.J. (2013). Hydrous
720 ringwoodite to 5 K and 35 GPa: Multiple hydrogen bonding sites resolved with
721 FTIR spectroscopy. American Mineralogist, 98, 637-642.

722 Peslier, A.H., 2010. A review of water contents of nominally anhydrous minerals in
723 the mantles of Earth, Mars and the Moon. Journal of Volcanology and
724 Geothermal Research, 197, 239-258.

725 Peslier, A.H., Woodland, A.B., Bell, D.R., and Lazarov, M. (2010) Olivine water
726 contents in the continental lithosphere and the longevity of cratons. Nature, 467,
727 78-U108.

728 Peslier, A., Schönbächler, M., Busemann, H., and Karato, S. (2017) Water in the
729 Earth's Interior: Distribution and Origin. Space Science Reviews, 212, 743-810.

730 Qin, T., Wentzcovitch, R.M., Umemoto, K., Hirschmann, M.M., and Kohlstedt, D.L.
731 (2018) Ab initio study of water speciation in forsterite: Importance of the
732 entropic effect. American Mineralogist, 103, 692-699.

733 Rychert, C.A., and Shearer, P.M. (2009) A global view of the
734 lithosphere–asthenosphere boundary. Science, 324, 495-498.

735 Smyth, J.R., Frost, D.J., Nestola, F., Holl, C.M., and Bromiley, G. (2006) Olivine
736 hydration in the deep upper mantle: effects of temperature and silica activity.
737 Geophysical Research Letters, 33, L15301.

738 Tauzin, B., Debayle, E., and Wittingger, C. (2010) Seismic evidence for a global
739 low-velocity layer within the Earth's upper mantle. Nature Geoscience, 3,
740 718-721.

741 Thoraval, C., Demouchy, S., and Padrón, J.A. (2018) Relative diffusivities of hydrous
742 defects from partially dehydrated natural olivine. Physics and Chemistry of
743 Minerals. DOI: https://doi.org/10.1007/s00269-018-0982-x.

744 Tollan, P.M.E., O'Neill, H.S.C., Hermann, J., Benedictus, A., and Arculus, R.J. (2015)
745 Frozen melt-rock reaction in a peridotite xenolith from sub-arc mantle recorded
746 by diffusion of trace elements and water in olivine. Earth and Planetary Science
747 Letters, 422, 169-181.

748 Tollan, P.M.E., O'Neill, H.S.C., and Hermann, J. (2018) The role of trace elements in
749 controlling H incorporation in San Carlos olivine. Contributions to Mineralogy
750 and Petrology, 173, 89.

751 Umemoto, K., Wentzcovitch, R.M., Hirschmann, M., Kohlstedth, D.L., and Withers,
752 A.C. (2011) A first-principles investigation of hydrous defects and IR frequencies
753 in forsterite: the case for Si vacancies. American Mineralogist, 96, 1475-1479.

754 Walker, A.M., Hermann, J., Berry, A., and O'Neill, H.S.C. (2007) Three water sites in
755 the upper mantle olivine and the role of titanium in the water weakening
756 mechanism. Journal of Geophysical Research, 112, B05211.

757 Wang, D.J., Mookherjee, M., and Xu, Y.S. (2006) The effect of water on the electrical
758 conductivity of olivine. Nature, 443, 977-980.

759 Wei, S.S., and Shearer, P.M. (2017) A sporadic low-velocity layer atop the 410-km
760 discontinuity beneath the Pacific Ocean. Journal of Geophysical Research, 122,
761 5144-5159.

762 Xia, Q.K., Liu, J., Kovács, I., Hao, Y.T., Li, P., Yang, X.Z., Chen, H., and Sheng, Y.M.
763 (2018) Water in the upper mantle and deep crust of eastern China: Concentration,
764 distribution and implications. National Science Review, doi:
765 10.1093/nsr/nwx016.

766 Xu, H., Zhao, Y., Hickmott, D.D., Lane, N.J., Vogel, S.C., Zhang, J., and Daemen, L.L.
767 (2013) High-temperature neutron diffraction study of deuterated brucite. Physics

768 and Chemistry of Minerals, 40, 799-810.

769 Xue, X., Kanzaki, M., Turner, D., and Loroch, D. (2017) Hydrogen incorporation
770 mechanisms in forsterite: New insights from 1H and 29Si NMR spectroscopy
771 and first-principles calculation. American Mineralogist, 102, 519-536.

772 Yang, X.Z., and Keppler, H. (2011) In-situ infrared spectra of OH in olivine to 1100℃.
773 American Mineralogist, 96, 451-454.

774 Yang, Y., Xia, Q., Feng, M., and Zhang, P. (2010) Temperature dependence of IR
775 absorption of OH species in clinopyroxene. American Mineralogist, 95,
776 1439-1443.

777 Yang, Y., Xia, Q., Feng, M., and Liu, S. (2012) OH in natural orthopyroxene: an in
778 situ FTIR investigation at varying temperatures. Physics and Chemistry of
779 Minerals, 39, 413-418.

780 Yang, Y., Xia, Q., and Zhang, P. (2015) Evolutions of OH groups in diopside and
781 feldspars with temperature. European Journal of Mineralogy, 27, 185-192.

782 Yang, Y., Ingrin, J., Xia, Q.K., and Liu, W.D. (2019) Nature of hydrogen defects in
783 clinopyroxenes from room temperature up to 1000 ^{o}C: Implication for the
784 preservation of hydrogen in the upper mantle and impact on electrical
785 conductivity. American Mineralogist, 104, 79-93.

786 Yoshino, T., Matsuzaki, T., Yamashita, S., and Katsura, T. (2006) Hydrous olivine
787 unable to account for conductivity anomaly at the top of the asthenosphere.
788 Nature, 443, 973-976.

789

790 **Figure captions**:

791 **Figure 1**. Polarized IR spectra at ambient conditions of the (a) natural olivine and (b)
792 synthetic Fe-free forsterite. The possible hydrogen sites responsible for the OH bands
793 are illustrated: (c) titanium-clinohumite defect; (d) pure Si vacancy. The yellow, blue

794 and gray balls represent oxygen, hydrogen and titanium atoms, respectively.

795 **Figure 2**. In situ IR spectra at elevated temperatures of the natural olivine: (a)
796 unpolarized spectra; (b) polarized spectra with the polarizer rotated at 0^o; (c) polarized
797 spectra with the polarizer rotated at 90^o. The spectra are normalized to 1 cm^{-1}
798 thickness and vertically offset. The arrows are to guide the eye.

799 **Figure 3**. In situ IR spectra at elevated temperatures of the synthetic forsterite: (a)
800 unpolarized spectra; (b) polarized spectra with the polarizer rotated at 0^o; (c) polarized
801 spectra with the polarizer rotated at 90^o. The spectra are normalized to 1 cm^{-1}
802 thickness and vertically offset. The arrows are to guide the eye.

803 **Figure 4**. In situ IR spectra with increasing pressure of the synthetic forsterite: (a)
804 polarized spectra with the polarizer rotated at 0^o; (b) polarized spectra with the
805 polarizer rotated at 90^o. The spectra are normalized to 1 cm^{-1} thickness and vertically
806 offset.

807 **Figure 5**. (a) The spectrum of the Si-O overtones of the nature olivine with the
808 polarizer rotated at 0^o, indicating that the spectrum was collected close to A axis
809 comparing with Asiow et al. (2006); (b) polarized IR spectra with the polarizer rotated
810 at 0^o of the natural olivine after annealing at 800 ^oC for different duration; (c)
811 polarized IR spectra with the polarizer rotated at 0^o of the natural olivine after 15
812 minutes of annealing at different temperatures; (d) The possible storage site
813 responsible for the newly occurred OH bands is illustrated: the blue, yellow and
814 purple balls represent hydrogen, oxygen and trivalent cations, respectively. The
815 spectra are normalized to 1 cm^{-1} thickness and vertically offset. The red dotted lines
816 denote the bands of increasing intensity with duration.

817 **Figure 6**. Evolutions of OH frequencies with increasing temperature: (a) olivine, the
818 circles and stars represent the natural olivine in this study and synthetic olivine from
819 Yang and Keppler (2011), respectively; (b) synthetic forsterite. The error bars of the
820 frequencies were obtained by performing multiple fitting of the spectra, and are
821 usually smaller than the symbol size.

822 **Figure 7**. Evolutions of (a) frequencies and (b) intensity ratio of the two intense bands
823 at 3610 and 3579 cm^{-1} with pressure. The error bars were obtained by performing
824 multiple fitting of the spectra.

825 **Figure 8**. (a) variations of the integral absorbances of the OH bands after annealing at
826 800 ^{o}C as a function of annealing duration. The error bars were obtained by
827 performing multiple fitting of the spectra; (b) fit of the data for hydrogen diffusivity at
828 800 ^{o}C using the one-dimensional model of diffusion. Errors were deduced from the
829 range of diffusivity values which can fit the data.

830 **Figure 9**. Illustrations of the interaction of hydrogen storage sites during
831 dehydrogenation with hydrogen released from titanium-clinohumite defects
832 transferring to the pure Si vacancy and trivalent cation defect. The yellow, gray and
833 purple balls represent oxygen, titanium, and trivalent cations, respectively.

834

835

836

837

838

839

840

841

842

843

844

845

846

This is a preprint, the final version is subject to change, of the American Mineralogist (MSA)
Cite as Authors (Year) Title. American Mineralogist, in press.
DOI: https://doi.org/10.2138/am-2019-6921

847

848 **Table 1.** OH band positions in the natural olivine and synthetic forsterite at various
849 temperatures and pressures, and intensity ratios of the 3610 to 3579 cm^{-1} band at
850 various pressures for the synthetic forsterite.

T/ ^{o}C	Frequency/cm^{-1}						
	Olivine			Forsterite			
20	3599(0)	3572(0)	3525(0)	3613(0.4)	3579(0.2)	3552(0.2)	3476(0.5)
100	3596(0)	3569(0)	3524(0)	3612(0.4)	3579(0.5)	3544(0)	3476(0)
200	3591(0)	3568(0)	3525(0)	3612(0.4)	3578(0.2)	3540(0)	3477(0.5)
300	3587(0)	3564(1)	3525(0)	3610(0.2)	3575(0.2)	3536(0.4)	3479(0.2)
400	3586(0)	3560(0)	3526(1)	3610(0.2)	3571(0.2)	3533(0.1)	3484(0)
500	3585(1)	3557(0.5)	3527(0)	3611(0.2)	3567(0.4)	3530(0)	3487(0.4)
600	3584(0.6)	3551(0.6)	3523(1)	3613(0.2)	3565(0.5)		
700		3547(0)		3611(0.2)	3565(0.5)		
800		3544(0)		3611(0.2)	3558(0.4)		
900				3611(0.2)	3556(0.4)		
1000					3556(0.4)		

	Forsterite		
P/GPa	Frequency/cm^{-1}		$I_{3610/3579}$
0	3612(0)	3578(0.7)	1.33(0.3)
0.86	3612(0)	3578(1.4)	1.71(0.5)
1.71	3612(0)	3577(0)	1.67(0.4)
2.76	3614(0)	3577(0.7)	2.78(0)
4.14	3615(0.7)	3576(2.1)	4.60(0.3)
7.04	3617(0.7)	3573(0.7)	3.42(0.7)
8.01	3618(0)	3574(2.1)	4.31(0.7)
9.36	3618(0)	3573(1.4)	4.77(0.9)
10.96	3619(0.7)	3572(2.8)	4.37(0.6)

851 **Notes**: We only show some prominent OH bands, especially at high temperature/pressure. The band positions and
852 intensities were determined by deconvoluting the spectra (original spectra not normalized to thickness) into
853 Gaussian components using the Peakfit program (ver. 4.12, Systat Software Inc.). The uncertainties in the brackets
854 were estimated by performing multiple fits on the spectra. The deconvolution is presented as an example in the
855 supplementary Figure S2. The deconvolution was performed on the in situ unpolarized IR spectra at various
856 temperatures, and performed on the in situ polarized 0^{o} IR spectra at various pressures.

857

This is a preprint, the final version is subject to change, of the American Mineralogist (MSA)
Cite as Authors (Year) Title. American Mineralogist, in press.
DOI: https://doi.org/10.2138/am-2019-6921

858

859 **Table 2.** Integral absorbances of OH bands of the natural olivine after annealing at
860 800 ^{o}C for different durations**.**

Duration (mins)	Ab_{3599} (cm^{-1})	Ab_{3572} (cm^{-1})	Ab_{3542} (cm^{-1})	Ab_{3524} (cm^{-1})
0	0.31746(0.009)	1.09639(0.129)	0.24427(0.007)	1.30739(0.056)
15	0.33474(0.017)	1.01843(0.095)	0.40989(0.003)	1.01697(0.067)
60	0.38807(0.047)	0.8084(0.081)	0.44474(0.006)	0.98808(0.022)
120	0.45085(0.001)	0.77598(0.009)	0.54574(0.049)	0.88639(0.072)
180	0.4447(0)	0.6976(0.136)	0.47976(0.032)	0.95994(0.040)
270	0.42928(0.032)	0.73(0)	0.6131(0)	0.81919(0)

861 **Notes**: Integral absorbance of each band was determined by deconvoluting the spectra (original spectra not
862 normalized to thickness) into Gaussian components using the Peakfit program (ver. 4.12, Systat Software Inc.).
863 The uncertainties in the brackets were estimated by performing multiple fits on the spectra. The deconvolution is
864 presented as an example in the supplementary Figure S3.

865

This is a preprint, the final version is subject to change, of the American Mineralogist (MSA)
Cite as Authors (Year) Title. American Mineralogist, in press.
DOI: https://doi.org/10.2138/am-2019-6921

Figure 1

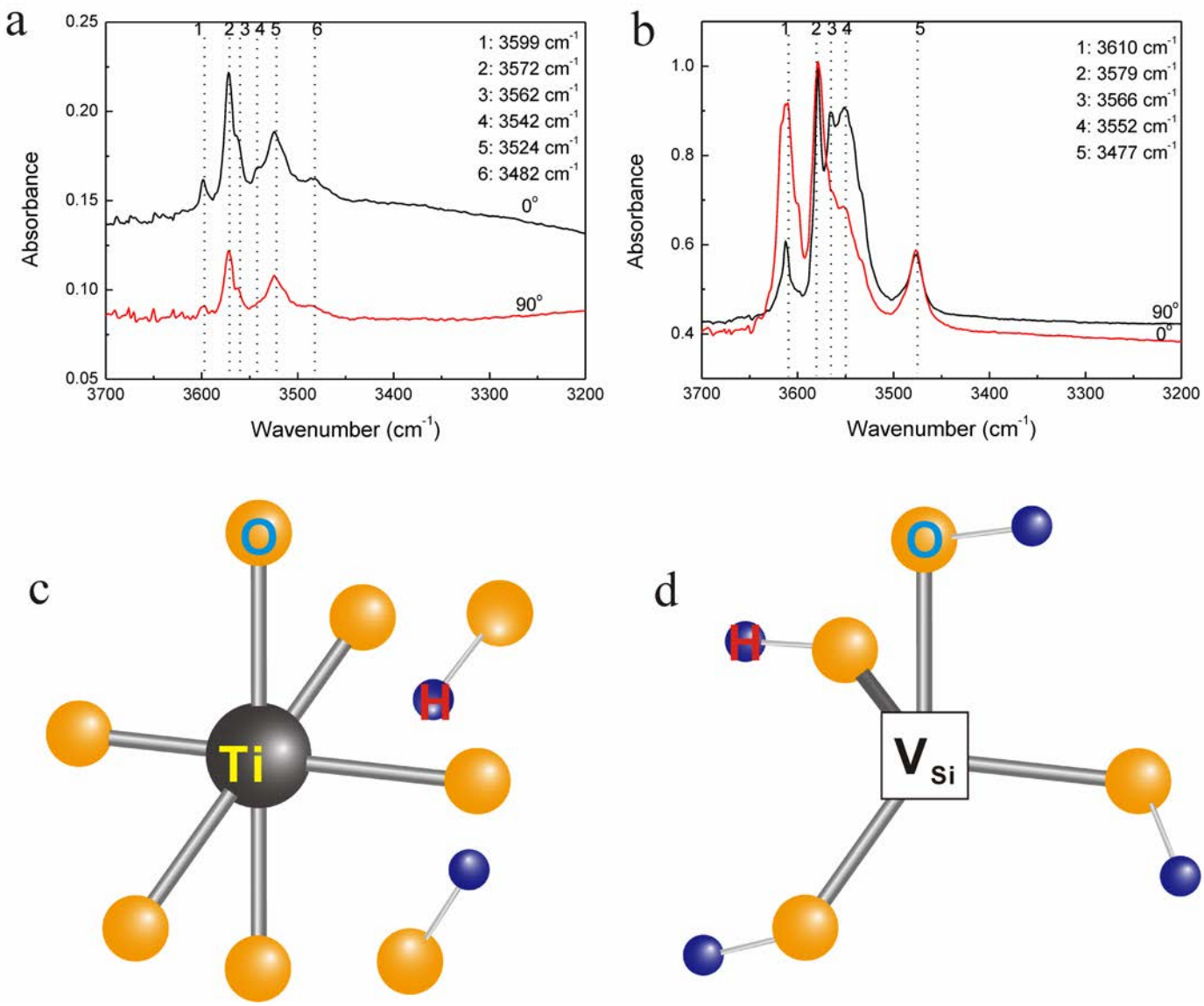

This is a preprint, the final version is subject to change, of the American Mineralogist (MSA)
Cite as Authors (Year) Title. American Mineralogist, in press.
DOI: https://doi.org/10.2138/am-2019-6921

Figure 2

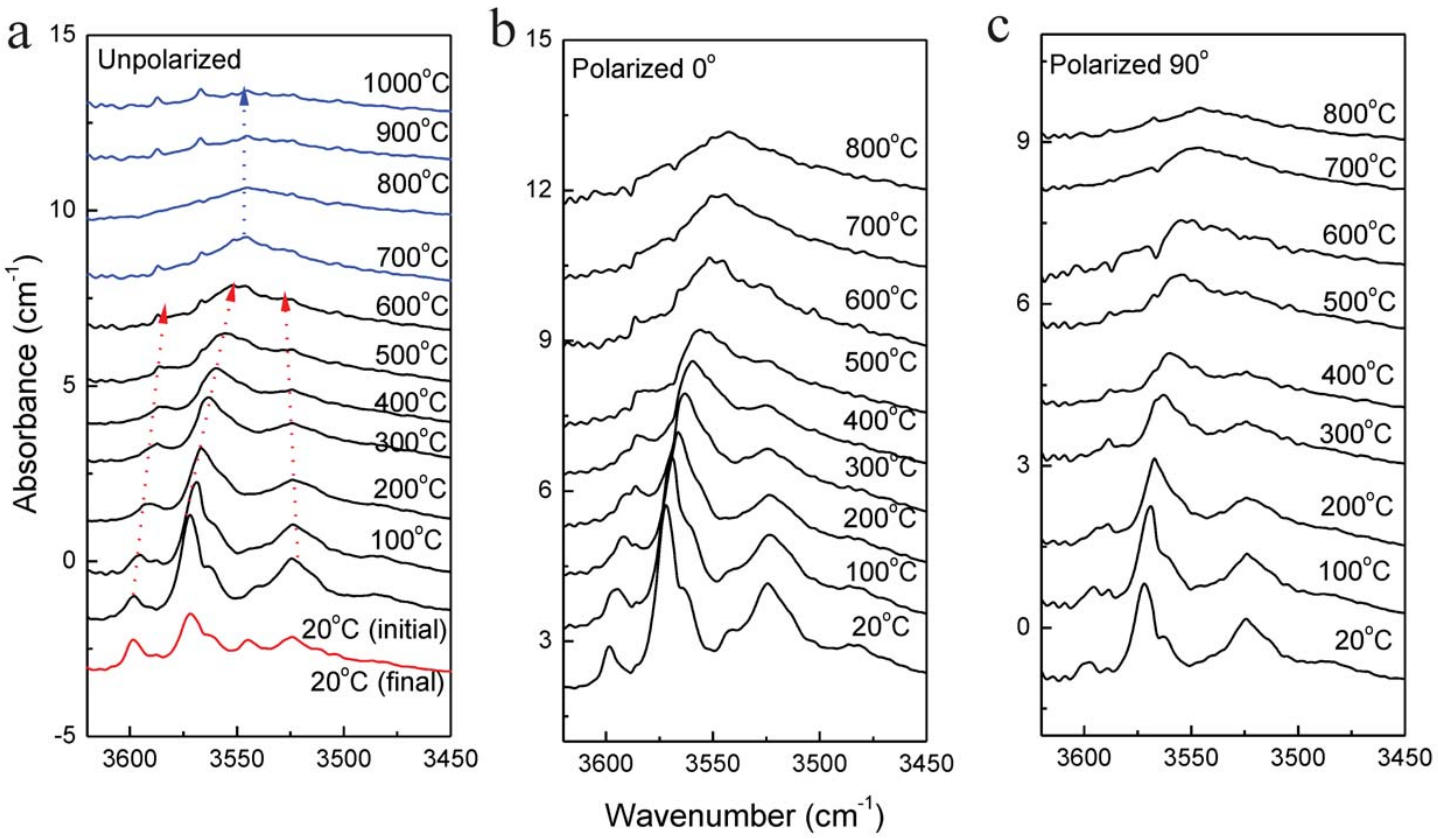

This is a preprint, the final version is subject to change, of the American Mineralogist (MSA)
Cite as Authors (Year) Title. American Mineralogist, in press.
DOI: https://doi.org/10.2138/am-2019-6921

Figure 3

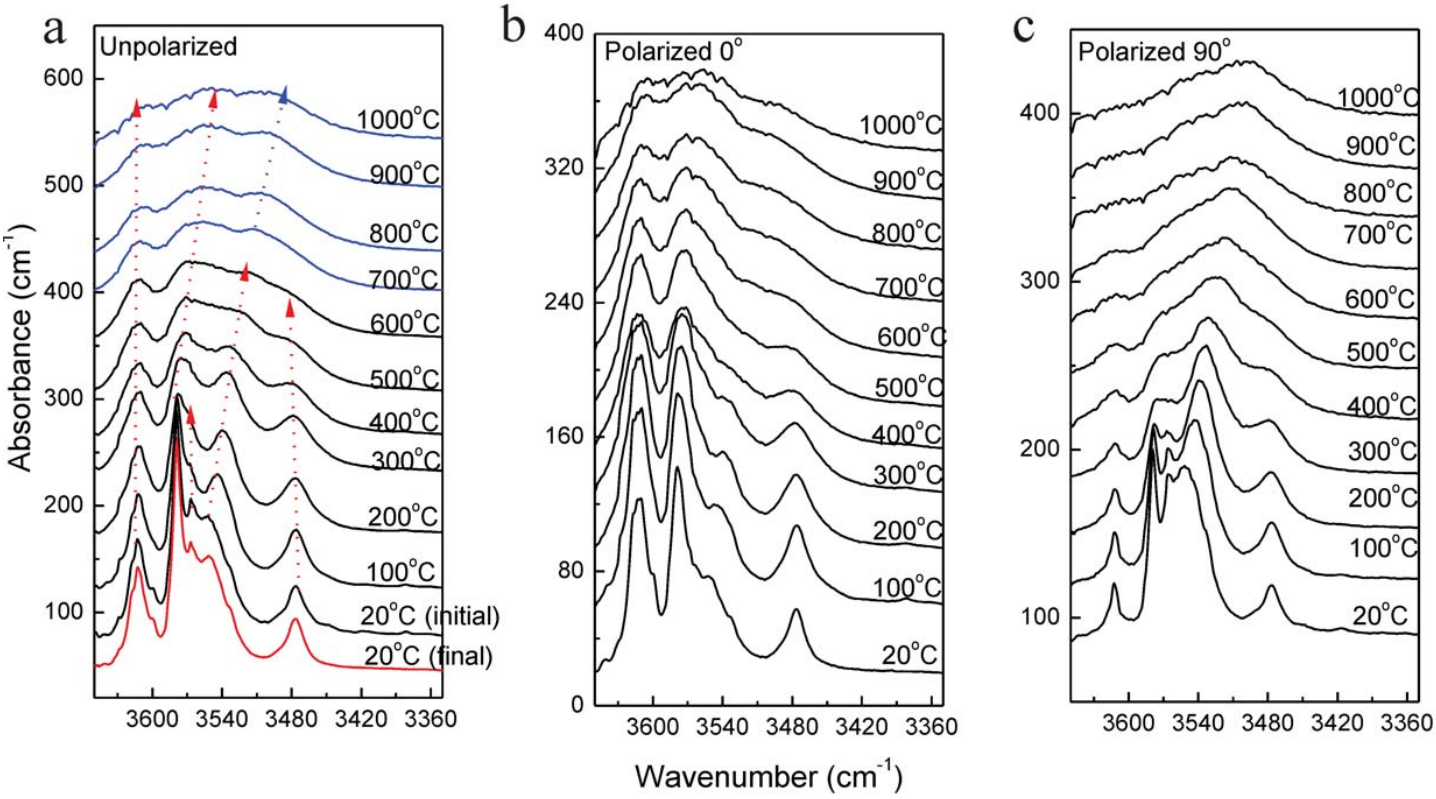

This is a preprint, the final version is subject to change, of the American Mineralogist (MSA)
Cite as Authors (Year) Title. American Mineralogist, in press.
DOI: https://doi.org/10.2138/am-2019-6921

Figure 4

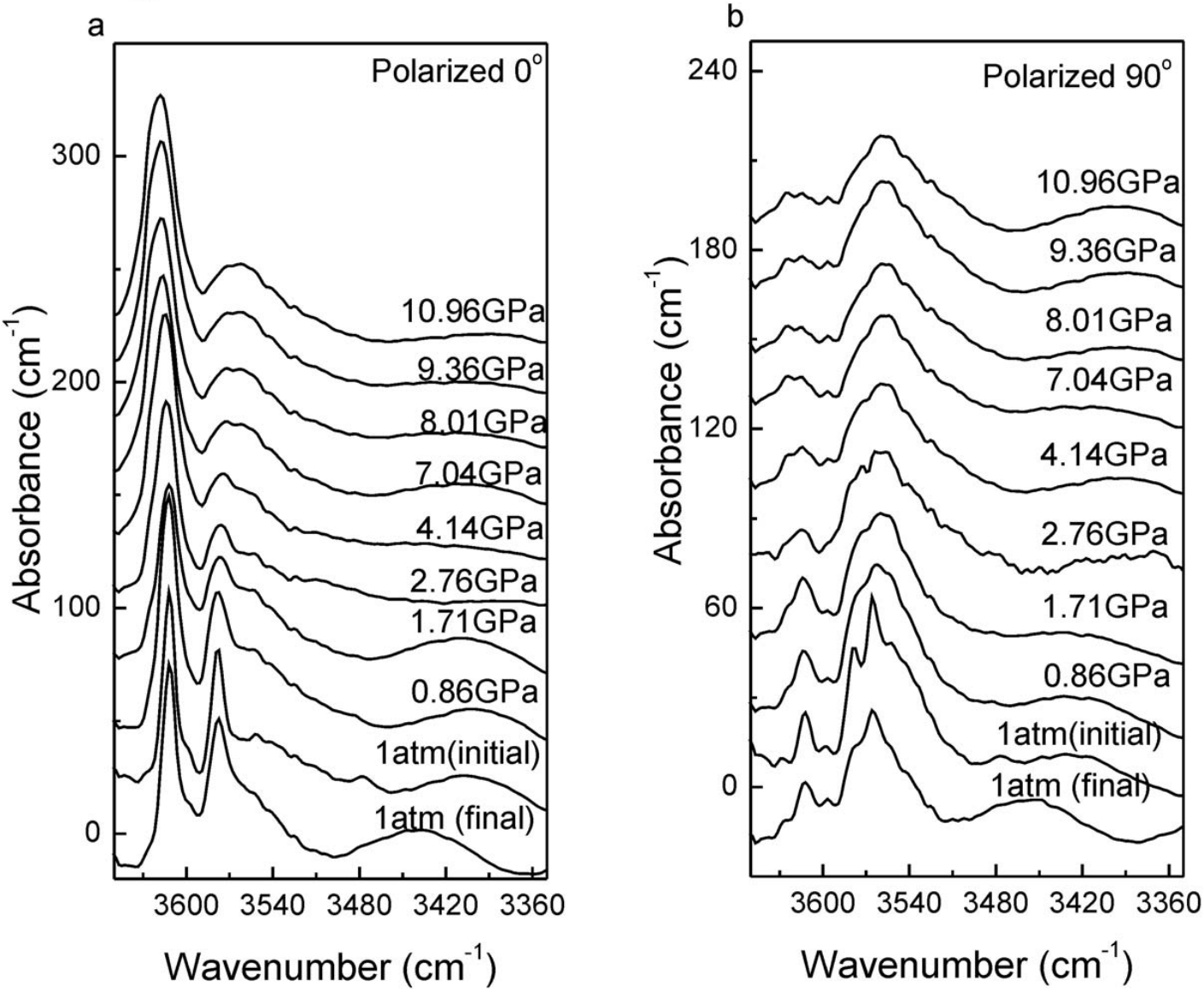

This is a preprint, the final version is subject to change, of the American Mineralogist (MSA)
Cite as Authors (Year) Title. American Mineralogist, in press.
DOI: https://doi.org/10.2138/am-2019-6921

Figure 5

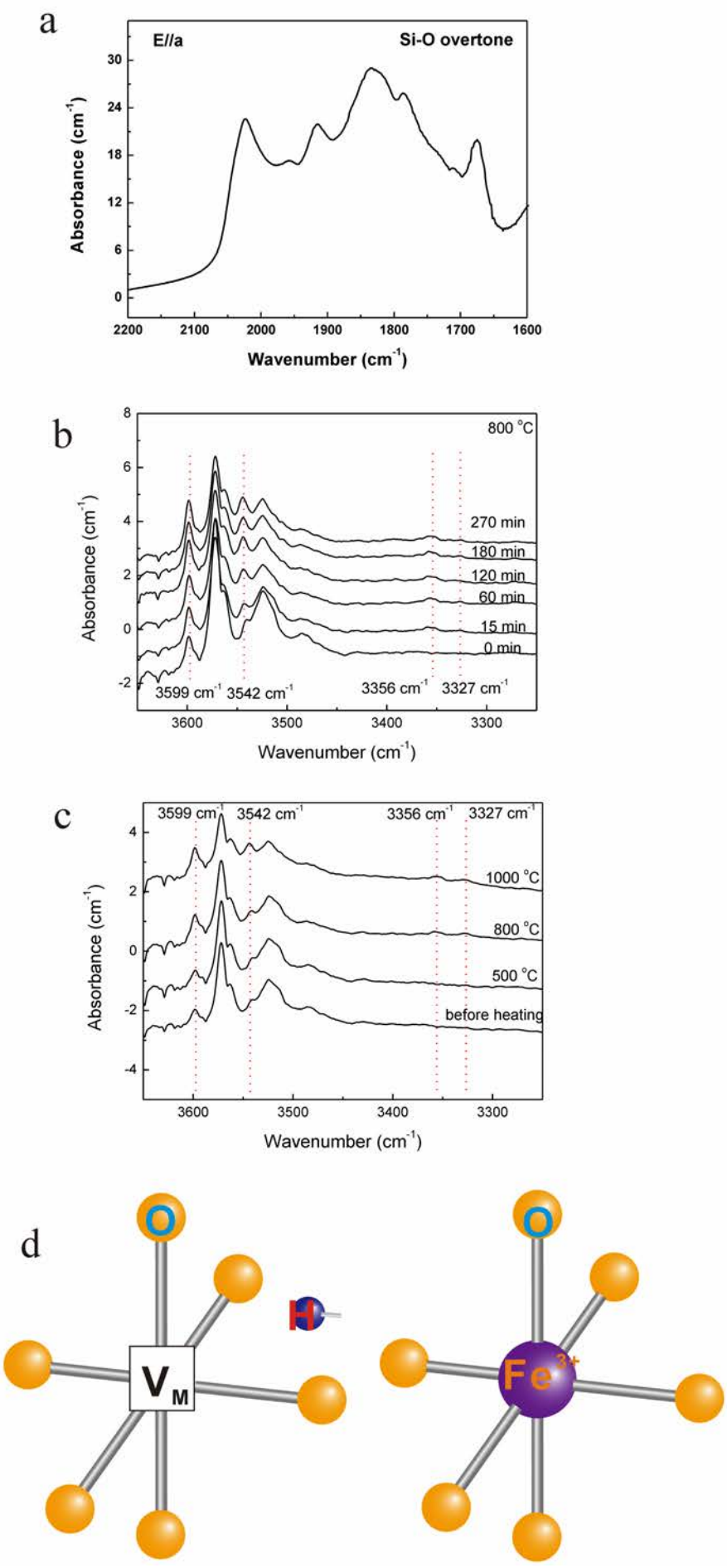

This is a preprint, the final version is subject to change, of the American Mineralogist (MSA)
Cite as Authors (Year) Title. American Mineralogist, in press.
DOI: https://doi.org/10.2138/am-2019-6921

Figure 6

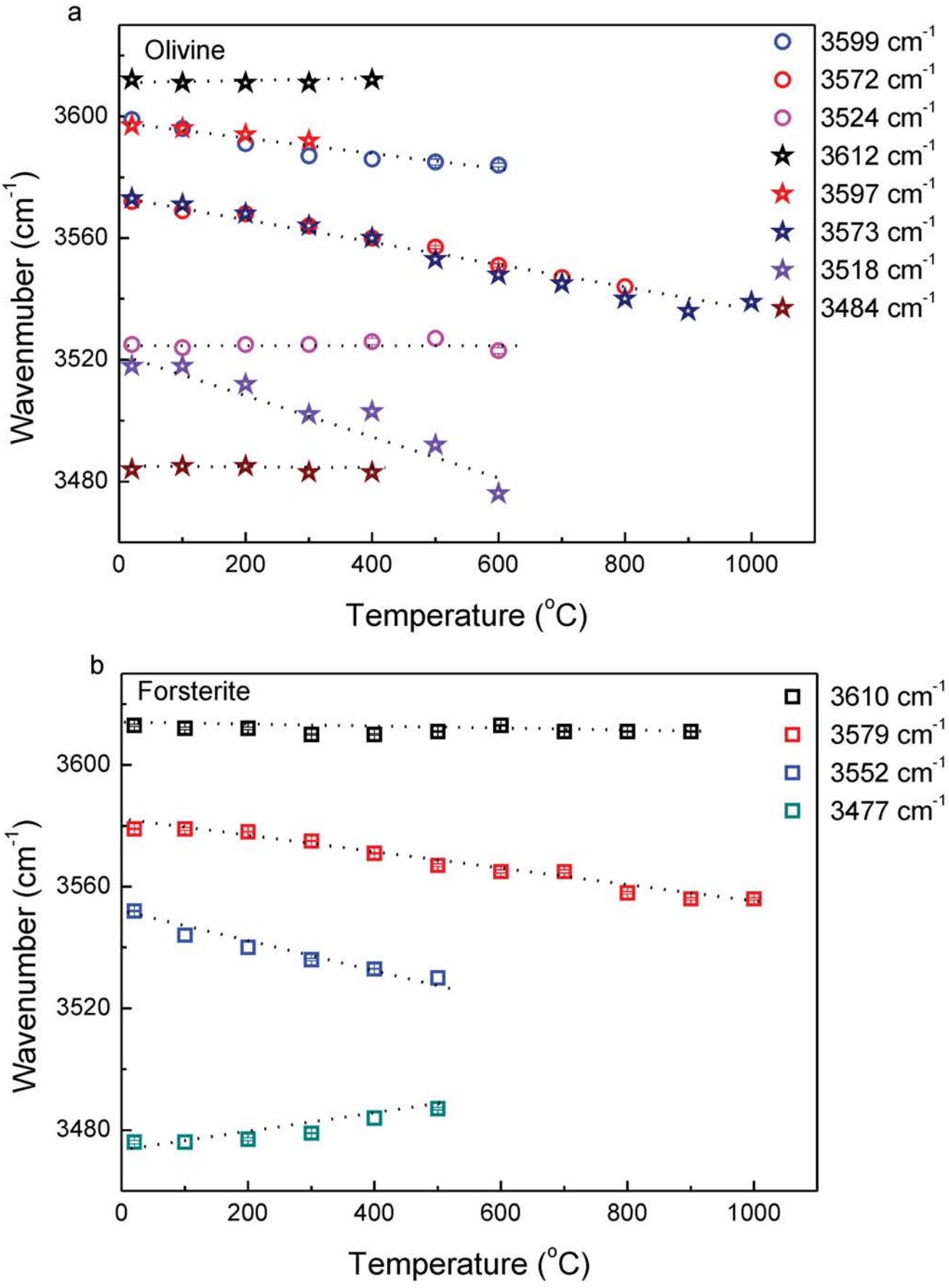

This is a preprint, the final version is subject to change, of the American Mineralogist (MSA)
Cite as Authors (Year) Title. American Mineralogist, in press.
DOI: https://doi.org/10.2138/am-2019-6921

Figure 7

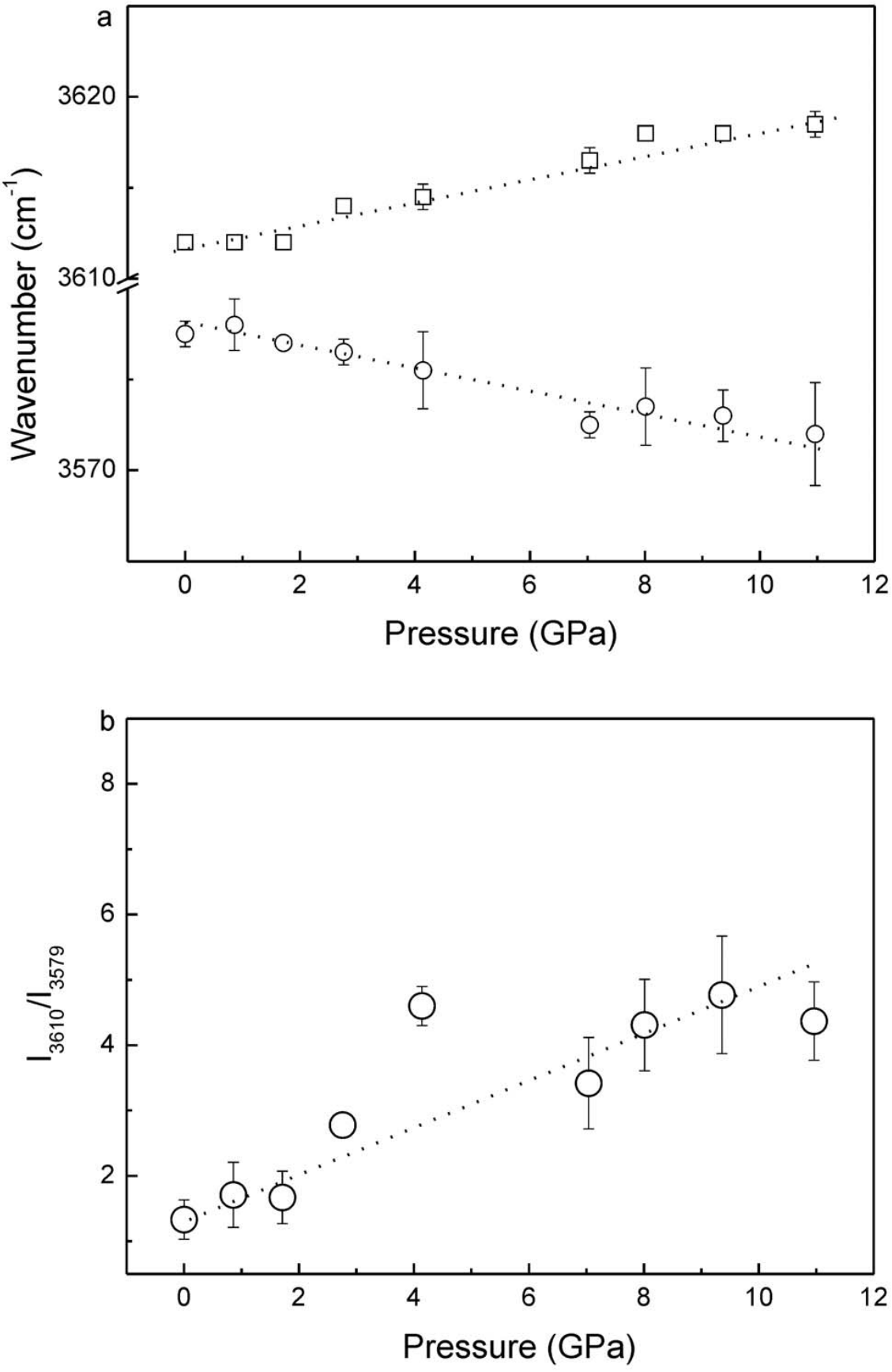

This is a preprint, the final version is subject to change, of the American Mineralogist (MSA)
Cite as Authors (Year) Title. American Mineralogist, in press.
DOI: https://doi.org/10.2138/am-2019-6921

Figure 8

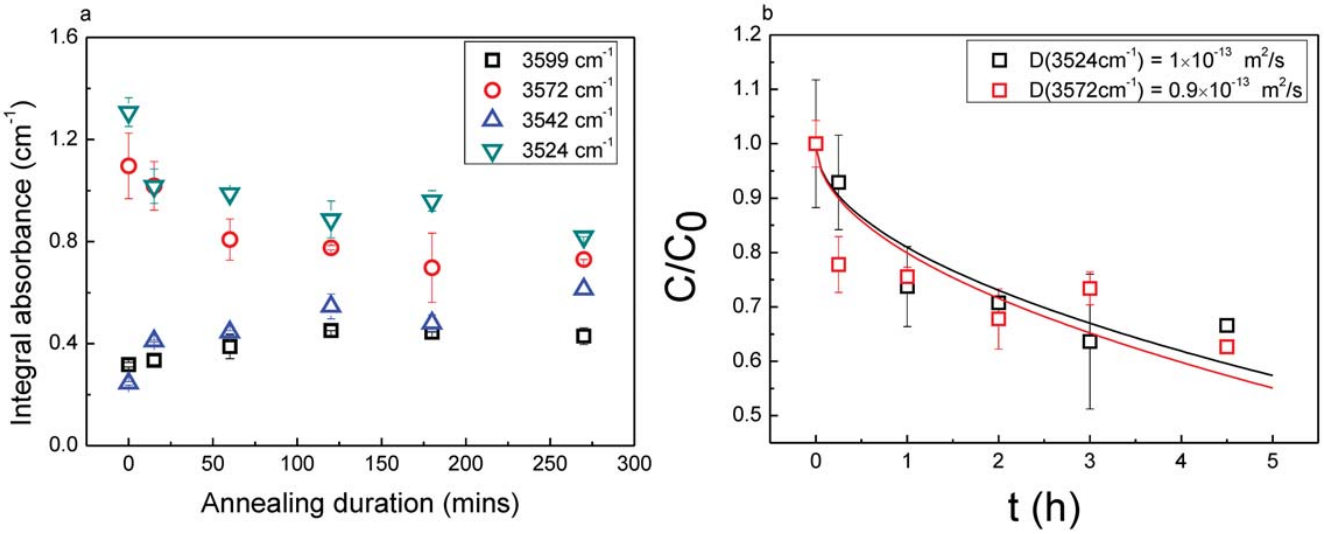

This is a preprint, the final version is subject to change, of the American Mineralogist (MSA)
Cite as Authors (Year) Title. American Mineralogist, in press.
DOI: https://doi.org/10.2138/am-2019-6921

Figure 9